17th Australasian Fluid Mechanics Conference

Auckland, New Zealand

5-9 December 2010

Prediction of Noise Induced by Low Mach Number Flows using a Hybrid CFD/BEM Approach

P. Croaker[1], N. Kessissoglou[1], D. Norrison[2], R. Widjaja[2] and G. Rosengarten[1]

[1]School of Mechanical and Manufacturing Engineering
The University of New South Wales, Sydney, Australia

[2] Maritime Platforms Division
Defence Science and Technology Organisation, Melbourne, Australia

Abstract

A hybrid CFD/BEM approach is proposed to extract the acoustic sources generated by low Mach number flow past a circular cylinder and to predict the associated far-field acoustic pressure. An incompressible computational fluid dynamics (CFD) solver is used to calculate the transient hydrodynamic flow field. Acoustic sources based on the linearised perturbed compressible equations (LPCE) are then extracted from the flow field data and combined with a boundary element method (BEM) model of a rigid circular cylinder to predict the sound pressure field. The spatial resolution of the extracted acoustic sources from an acoustic perspective is much finer than required, which may lead to inefficiencies in the BEM analysis. In this work, a method is developed to spatially condense the acoustic sources extracted from the CFD data to reduce the number of acoustic sources, while preserving the accuracy of the predicted sound pressure field. The results from this hybrid CFD/BEM approach are presented for flow past a circular cylinder with Reynolds number, Re_D=100 and Mach number, M=0.15. The directivity of the radiated sound pressure field at the vortex shedding frequency agrees well with results of alternate methods available in the literature. The spatial condensation method is shown to produce good accuracy provided the particle spacing is sufficient to preserve the phase relationship between nearby acoustic sources.

Introduction

Two main groups of hybrid methods are commonly used to derive acoustic sources from a CFD flow field and predict the propagation of these acoustic sources to the far field. Methods in the first group are based on Lighthill's acoustic analogy [1, 2] and solve the CFD and sound propagation in a decoupled manner. The acoustic sources are extracted from the transient flow field data and then a wave equation, derived from Lighthill's acoustic analogy [1, 2], is solved to predict the propagation of these acoustic sources. Lighthill's original work considered the propagation of acoustic waves from unbounded turbulent flows. Curle [3] extended Lighthill's acoustic analogy to include the effect of stationary, impermeable rigid surfaces on the sound propagation. The work of Ffowcs Williams and Hawkings [4] allowed for the impermeable rigid surfaces to be in arbitrary motion and di Francescantonio [5] further extended this to allow the surfaces to be permeable. Methods in the second group are based on the splitting of the solution variables into both hydrodynamic and acoustic components. This leads to two sets of equations to be solved. One set of equations resolves the unsteady baseline hydrodynamic flow field while the other set of equations resolves the acoustic perturbations of the solution variables around this baseline flow. Using this approach the hydrodynamic and acoustic equations are solved simultaneously with the hydrodynamic solution influencing the propagation of waves in the acoustic simulation. Methods that fall into this second group include the expansion about incompressible flow (EIF) method of Hardin and Pope [6], the acoustic perturbation equation method of Ewert and Schröder [7], the perturbed compressible equations (PCE) and the linearised perturbed compressible equations (LPCE) methods of Seo and Moon [8, 9].

The LPCE method was developed to suppress the generation of 'perturbed vorticity' due to coupling between the incompressible flow variables and the perturbed acoustic quantities. Perturbed vorticity was shown to cause inaccuracies and instabilities with the EIF and PCE methods [8, 9]. The LPCE method has been shown to accurately predict the sound pressure field radiated from laminar flow [9] and turbulent flow [10] past a cylinder. One of the features of the LPCE is that the only acoustic source term is the material derivative of the hydrodynamic pressure.

A hybrid CFD/BEM method has recently been developed by the authors to extract acoustic sources from incompressible transient CFD data based on the LPCE source terms [11]. The propagation of these acoustic sources is then calculated using a BEM solver. The BEM solver also contains a finite element method (FEM) solver that is able to simulate the vibro-acoustic response of structures. Coupling these BEM and FEM solvers together allows the effect of fluid/structure interaction on the sound propagation to be determined. Hence, the hybrid CFD/BEM method can be extended to consider the interaction of flow-induced noise with a flexible marine vessel and predict the resulting far field radiated sound. The method developed in Ref. [11] creates one acoustic monopole source at the centre of each CFD cell. For wall bounded turbulent flows, a large number of acoustic sources will be created that will subsequently result in a very slow BEM analysis. In the present work a method is developed to spatially condense the acoustic source data extracted from the CFD simulation and thereby reduce the number of monopole sources used in the BEM simulation. The spatial condensation method is a mesh-free method and involves overlaying a distribution of particles on the CFD mesh. The spatial resolution of these particles is coarser than the CFD mesh. Each particle has a radius of influence and the total acoustic source of each particle is calculated by summation of the CFD cell acoustic sources within this radius of influence, weighted by distance to the particle. An acoustic monopole source is then created for each particle and used in the BEM analysis.

The aim of this work is to extract the acoustic sources generated by low Mach number flow past a cylinder, predict the radiated sound pressure with and without spatial condensation and assess

the accuracy of the method. This new hybrid CFD/BEM approach is applied to predict the far-field sound pressure induced by the laminar flow past a cylinder at a Reynolds number, Re_D=100 and Mach number, M=0.15. The successful outcomes of this work have application to marine vessels, in order to predict the excitation of a ship or submarine hull due to pressure fluctuations from the propeller.

Numerical Methods

Linearised Perturbed Compressibility Equations

In the LPCE method, the total flow variables are decomposed into incompressible and perturbed components:

$$\rho = \rho_0 + \rho'$$
$$\mathbf{u} = \mathbf{U} + \mathbf{u}' \quad (1)$$
$$p = P + p'$$

where ρ is the total fluid density, ρ_0 is the density of the incompressible fluid and ρ' is the density perturbation. Similarly $\mathbf{u}$ is the total velocity vector of the fluid, where $\mathbf{U}$ and $\mathbf{u}'$ are respectively the incompressible and perturbed velocity vectors, and p is the total static pressure of the fluid, with P and p' representing the incompressible and perturbed components of static pressure, respectively. The LPCE are given by:

$$\frac{\partial \rho'}{\partial t} + (\mathbf{U}\cdot\nabla)\rho' + \rho_0(\nabla\cdot\mathbf{u}') = 0 \quad (2)$$

$$\frac{\partial \mathbf{u}'}{\partial t} + \nabla(\mathbf{u}'\cdot\mathbf{U}) + \frac{1}{\rho_0}\nabla p' = 0 \quad (3)$$

$$\frac{\partial p'}{\partial t} + (\mathbf{U}\cdot\nabla)p' + \gamma P(\nabla\cdot\mathbf{u}') + (\mathbf{u}'\cdot\nabla)P = -\frac{DP}{Dt} \quad (4)$$

where γ is the ratio of specific heats. The term on the right hand side of equation (4) is the material derivative of the hydrodynamic pressure and is given by:

$$\frac{DP}{Dt} = \frac{\partial P}{\partial t} + \mathbf{U}\cdot\nabla P \quad (5)$$

This material derivative of pressure is the only acoustic source term in the LPCEs. Equation (2) is the linearised continuity equation. Equations (3) and (4) are the linearised conservation of momentum and conservation of energy equations, respectively. Seo and Moon [9] derived a wave equation for the Perturbed Compressible Equations (PCE) method. Using this wave equation as a starting point, a wave equation for the LPCE is:

$$\nabla^2 p' - \frac{1}{c_0^2}\frac{\partial^2 p'}{\partial t^2} - \frac{1}{c_0^2}(\mathbf{U}\cdot\nabla)\frac{\partial p'}{\partial t} - \frac{1}{c_0^2}\left(\frac{\partial \mathbf{U}}{\partial t}\cdot\nabla\right)p'$$
$$-\frac{1}{c_0^2}\left(\frac{\partial \mathbf{u}'}{\partial t}\cdot\nabla\right)P - \frac{1}{c_0^2}(\mathbf{u}'\cdot\nabla)\frac{\partial P}{\partial t} - \frac{\gamma}{c_0^2}\frac{\partial P}{\partial t}(\nabla\cdot\mathbf{u}') \quad (6)$$
$$+\rho_0\nabla\cdot\nabla(\mathbf{u}'\cdot\mathbf{U}) = \frac{1}{c_0^2}\frac{\partial}{\partial t}\left(\frac{DP}{Dt}\right)$$

where the relationship $\gamma P = \rho_0 c^2$ has been used. The term on the right hand side corresponding to $\frac{1}{c_0^2}\frac{\partial}{\partial t}\left(\frac{DP}{Dt}\right)$ is the acoustic source term from the LPCE and will be extracted from an incompressible CFD simulation. The terms on the left hand side of equation (6) resolve the propagation of the acoustic sources. In the hybrid method developed here, a standard inhomogeneous wave equation convected by a uniform flow is used to predict the acoustic propagation. For a uniform flow velocity, $\mathbf{U} = (U_x, 0, 0)$, the standard inhomogeneous convective wave equation, with source term derived from the LPCE method, is given by:

$$\nabla^2 p' - \frac{1}{c_0^2}\frac{\partial^2 p'}{\partial t^2} - \frac{2M}{c_0}\frac{\partial^2 p'}{\partial x \partial t} - M^2\frac{\partial^2 p'}{\partial x^2} = \frac{1}{c_0^2}\frac{\partial}{\partial t}\left(\frac{DP}{Dt}\right) \quad (7)$$

where $M = U_x/c_0$ is the Mach number. Notwithstanding the simplifying assumption of uniform mean flow in equation (7), a comparison of equations (6) and (7) reveals that a number of terms from equation (6) have been set to zero. These terms are acoustic scattering terms relating to the mean flow having a refraction effect which is negligible at low Mach numbers. Seo and Moon [9] show that the Mach number dependence of these terms are $O(M^3)$ or higher, whereas the leading order terms are $O(M)$.

It is worth noting that although a uniform velocity field is assumed for the convection of the acoustic waves, no such simplification is required for the acoustic source term. The acoustic source data is extracted from a transient CFD simulation and hence the velocity field used to calculate the acoustic source term is both spatially and temporally varying.

Equation (7) is very similar to the acoustic analogy of Ribner [12]. The only difference being the source term in Ribner's analogy is given by $\frac{1}{c_0^2}\frac{D^2P}{Dt^2}$ instead of $\frac{1}{c_0^2}\frac{\partial}{\partial t}\left(\frac{DP}{Dt}\right)$. Equation (8) reveals the difference between the source term considered in the present work and with Ribner's source term:

$$\frac{1}{c_0^2}\frac{D^2P}{Dt^2} = \frac{1}{c_0^2}\frac{\partial}{\partial t}\left(\frac{DP}{Dt}\right) + \frac{1}{c_0^2}(\mathbf{U}\cdot\nabla)\frac{DP}{Dt} \quad (8)$$

The right hand side of equation (8) shows that the source term from Ribner's acoustic analogy contains an additional term, $\frac{1}{c_0^2}(\mathbf{U}\cdot\nabla)\frac{DP}{Dt}$, when compared with the acoustic source considered here. The results obtained using the two different source terms from the present method and the acoustic analogy of Ribner will be compared in future work.

Transient Laminar CFD Simulation

Laminar vortex shedding from a cylinder of diameter D is simulated at Re_D=100 and M=0.15. For this simulation a two-dimensional circular domain around the cylinder has been modelled and analysed using ESI Group's CFD-ACE+ software package [13]. The velocity-pressure form of the Navier-Stokes equations are solved by CFD-ACE+ and in this instance a direct numerical simulation (DNS) of the flow field has been performed. The Navier-Stokes equations are given by:

$$\frac{\partial(\rho U_x)}{\partial t} + \nabla\cdot(\rho\mathbf{U}U_x) = -\frac{\partial p}{\partial x} + \nabla\cdot(\mu\nabla U_x) + S_{Mx}$$
$$\frac{\partial(\rho U_y)}{\partial t} + \nabla\cdot(\rho\mathbf{U}U_y) = -\frac{\partial p}{\partial y} + \nabla\cdot(\mu\nabla U_y) + S_{My} \quad (9)$$
$$\frac{\partial(\rho U_z)}{\partial t} + \nabla\cdot(\rho\mathbf{U}U_z) = -\frac{\partial p}{\partial z} + \nabla\cdot(\mu\nabla U_z) + S_{Mz}$$

where $\mathbf{U} = (U_x, U_y, U_z)$ is the velocity vector and S_{Mx}, S_{My} and S_{Mz} are momentum source terms in the x, y and z directions, respectively. CFD-ACE+ uses an iterative, segregated solution method with the pressure-velocity coupling handled using the SIMPLEC algorithm.

The model used for the CFD simulation is shown in Figure 1, with the mesh topology in the vicinity of the cylinder inset. The interior of the computational domain extends radially for 25*D*. A 'sponge' layer extends radially for an additional 20*D*. The interior domain contains 71,760 quadrilateral cells, with a cell spacing adjacent to the cylinder of 0.005*D*. The cell distribution is biased so that the wake region contains a high cell density to resolve the vortices shed from the cylinder. The sponge layer contains an additional 6,960 quadrilateral cells. The cell size on either side of the interface between the interior domain and sponge layer is uniform, with the cells in the sponge layer then growing rapidly in the radial direction.

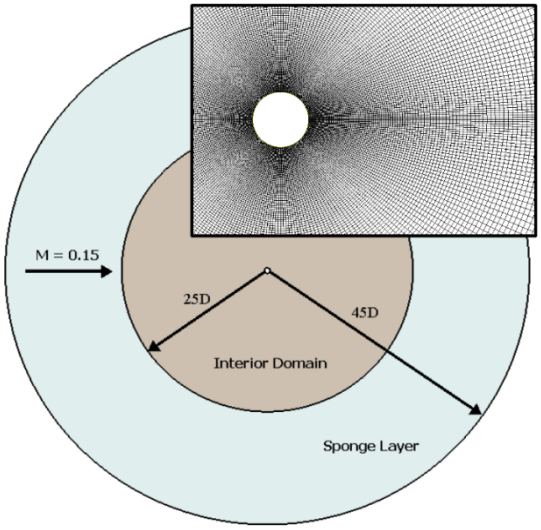

Figure 1. Domain shape and size for CFD analysis

In the sponge layer the viscosity has been artificially increased to damp out the fluctuations in the velocity field. The rapid growth of cell size away from the interior domain/sponge layer interface, combined with the step change in viscosity at the interface may introduce numerical artifacts. The presence of any such artifacts or their effect on the solution has not been investigated in this work.

A convective boundary condition was also applied to the outlet boundary to reduce reflection of vorticity back into the computational domain. The convective boundary condition, based on the Sommerfeld radiation condition, was first proposed by Orlanski [14] and has been successfully applied to transient CFD simulations involving vortex shedding [15, 16]. This boundary condition takes the form:

$$\frac{\partial u_i}{\partial t} + U_{conv}\frac{\partial u_i}{\partial n} = 0 \qquad (10)$$

where U_{conv} is the convection velocity normal to the boundary and $\frac{\partial u_i}{\partial n}$ represents the gradient of the i^{th} component of velocity normal to the outlet boundary.

A steady state simulation was performed with the converged solution used as the initial condition of the transient simulation. The simulations were second order accurate in time and space, with a central difference scheme used for the spatial discretisation and a Crank-Nicholson scheme used for the temporal discretisation. The transient simulation was executed for 40,000 time steps with the time step size given by 0.0478*tU*/*D*. This is equivalent to a time step of 4.78E-4s and is sufficient to capture approximately 300 vortex shedding periods. The simulation was allowed to progress until the flow field achieved periodicity. Recording of the acoustic source data commenced after this periodicity had been attained.

Boundary Element Method

The Boundary Element solver in ESI Group's vibro-acoustic simulation package, VA One 2010, is used to solve the acoustic propagation [17]. This boundary element method solves the harmonic wave (Helmholtz) equation and is able to consider the effects of uniform mean flow on sound propagation.

Taking the Fourier transformation in time of equation (7), the Helmholtz equation can be expressed as:

$$\nabla^2 p' + k^2 p' - 2ikM\frac{\partial p'}{\partial x} - M^2\frac{\partial^2 p'}{\partial x^2} = S \qquad (11)$$

where S is the acoustic source, $k(=\omega/c)$ is the wave number, ω is the harmonic radian frequency and $M = U_x/c_0$ is the Mach number. The boundary element model is driven by acoustic monopoles which are derived from the acoustic sources extracted from the transient CFD data. At each time step the acoustic source term generated in each CFD cell is given by:

$$S_n^i = \frac{1}{c_0^2}\frac{\partial}{\partial t}\left(\frac{DP_n^i}{Dt}\right) \qquad (12)$$

where S_n^i is the acoustic source density of the i^{th} CFD cell at time step n, with units of Pa.m^{-2}. This results in a time history of the acoustic source density for each CFD cell. The approach that has been adopted in the present work creates an acoustic monopole at the centre of each CFD cell and uses the acoustic source density to derive the complex frequency spectrum that defines each monopole.

In VA One 2010, an expression to determine the RMS pressure caused by an acoustic monopole source is given by:

$$p_{rms}(r,\omega) = \frac{|A(\omega)|}{4\pi r} \qquad (13)$$

where $|A(\omega)|$ is the modulus of the complex spectrum that defines the monopole and has units Pa.m. It is important to note that the monopole is a point source, whereas S_n^i represents the acoustic source strength per unit volume. Hence the acoustic source density extracted from the CFD results must be multiplied by the CFD cell volume to give the total acoustic source acting at the cell centre:

$$R_n^i = S_n^i V^i \qquad (14)$$

where R_n^i is the total acoustic source acting at the centre of the i^{th} cell at time step n and V^i is the volume of the i^{th} cell.

Spatial Condensation of Acoustic Source Data

The method outlined in the preceding sections creates an acoustic monopole for each CFD cell. For wall bounded turbulent flows, this will result in a large number of acoustic sources which will significantly slow the subsequent BEM analysis. To speed up the solution process, a method has been developed in which the acoustic source data is spatially condensed. This method is described in what follows.

Figure 2 shows a schematic diagram of the spatial condensation method that has been developed. Concentric rings of particles are overlaid on the CFD mesh. The distribution of these particles is defined by the radius of the concentric rings, *r*, the distance separating particles on the same concentric ring, *d*, and the radial distance between adjacent rings, *dr*. Another important parameter

is the radius of influence of each particle, l. The acoustic sources of all CFD cells that lie within the radius of influence of a particular particle are weighted by distance to the particle. These weighted acoustic sources are then summed together to give the total acoustic source of that particle. A variety of weighting functions can be implemented, however in the present work a Gaussian kernel has been used to calculate the distance based weighting. The Gaussian weighting applied to the i^{th} CFD cell by the k^{th} particle is calculated using the following equation:

$$w_{i,j} = \exp(-x_{i,j}^2 / 2\sigma^2) \tag{15}$$

where σ is a smoothing parameter that influences the shape of the Gaussian kernel and $x_{i,k}$ is given by:

$$x_{i,k} = \frac{y_{i,k}}{d} \tag{16}$$

$y_{i,k}$ is the distance between the i^{th} CFD cell centre and the k^{th} particle and d is the distance separating adjacent particles on the same concentric ring, with d a function of concentric ring radius, r.

Figure 3 shows the Gaussian kernels of three adjacent particles and highlights how the distanced based weighting is calculated for the i^{th} CFD cell.

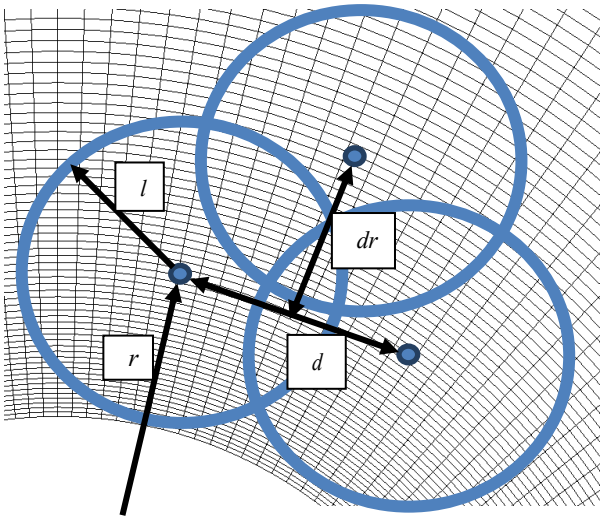

Figure 2. Particles overlaid on CFD mesh

Figures 2 and 3 demonstrate that a CFD cell may lie within the radius of influence of multiple particles. The sum of the weightings applied to the i^{th} CFD cell is determined by:

$$W_i = \sum_{k=1}^{M} w_{i,k} \tag{17}$$

For the applied method to be globally conservative, $W_i = 1$ for each CFD cell. To ensure this condition, a scaling factor is defined for each CFD cell:

$$C_i = \frac{1}{W_i} \tag{18}$$

Using these scaling factors and the Gaussian weightings, the globally conservative acoustic source time histories for the particles is calculated by:

$$R_n^k = \sum_{i=1}^{P} C_i w_{i,k} R_n^i \tag{19}$$

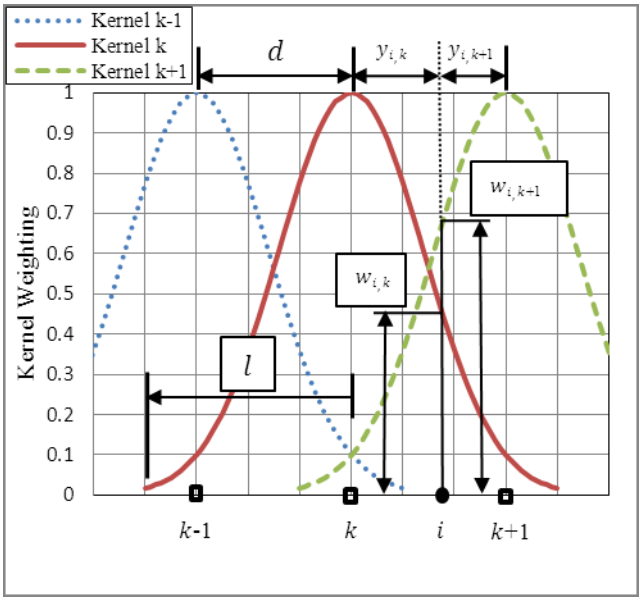

Figure 3. Weighting of i^{th} CFD cell to adjacent particles

Digital Signal Processing of Acoustic Source Data

To convert the acoustic source time histories into frequency spectra, a discrete Fourier transform (DFT) must be performed. The DFT assumes that the finite length time history is one period of an infinitely long periodic signal which requires $R_0^i = R_N^i$, where N is the final time step of the simulation. If this condition is not met, 'spectral leakage' occurs which pollutes the frequency spectra. For laminar vortex shedding from a cylinder it is relatively straightforward to specify a total simulation time that is an integer multiple of the vortex shedding period, thus ensuring that $R_0^i = R_N^i$. However the method developed herein will ultimately be applied to wall-bounded turbulent flows. While it may be possible to capture the periodicity of the large scale structures in such a flow, the smaller scale turbulent fluctuations may not exhibit any periodicity and hence a more robust approach based on Welch's modified periodogram method [18] is used.

The acoustic source time history of each CFD cell is divided into equal segments and multiplied by a Hanning window function to enforce periodicity of each segment. The frequency spectra of each segment are then computed using the *four1* and *realft* fast Fourier transform (FFT) algorithms of Press et al. [19]. An implementation of Welch's modified periodogram method [18] is programmed in Fortran 95 and used to calculate average power and cross spectrum for each acoustic source, with the cross spectrum calculated relative to the spectrum at top-dead centre of the cylinder. The power and cross spectrum for each acoustic source is converted to a complex pressure spectrum which is used to define the acoustic monopole at each CFD cell centre.

Results and Discussion

Hydrodynamic Results

Figure 4 shows a plot of the vorticity in the flow field at one instance in time. The vorticity generated at the cylinder surface is shed from the cylinder and travels downstream as vortex pairs.

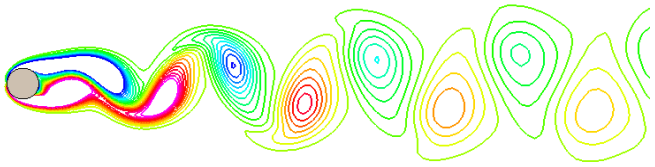

Figure 4. Vorticies in wake of cylinder

Figure 5 shows the frequency spectra of the fluctuating lift and drag forces exerted on the cylinder. The fundamental vortex shedding frequency is identified to be 16.3 Hz. This figure also illustrates that peaks of the fluctuating lift force occur at odd harmonics of the vortex shedding frequency and peaks of the drag force occur at even harmonics.

The mean drag coefficient calculated from the transient CFD simulation is C_D=1.32 which compares well with the experimental value of 1.24-1.26 obtained by Tritton [20]. The Strouhal number predicted from the present analysis is St=0.163, which compares well with the experimental value of 0.164 reported by Fey et al. [21].

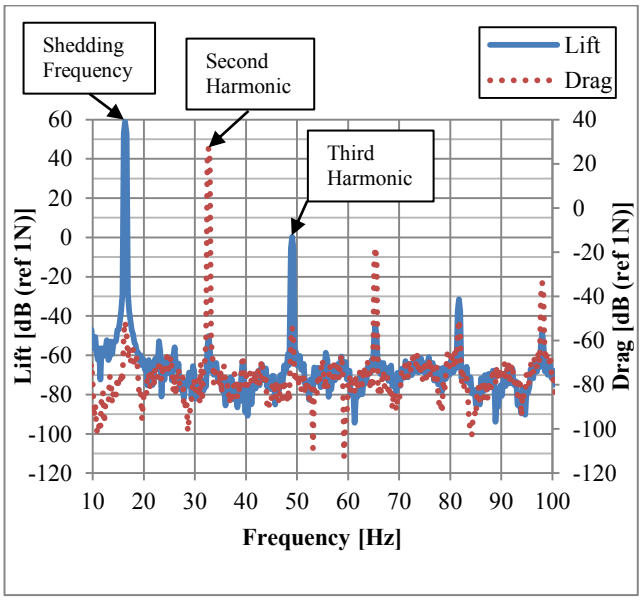

Figure 5. Frequency spectra of lift and drag forces

Based on published simulation data for laminar shedding from circular cylinders in cross flow, Norberg [22] developed the following empirical relationship to approximate the RMS of the fluctuating lift force:

$$C_{L'} = \sqrt{\left(\frac{\epsilon}{30} + \frac{\epsilon^2}{90}\right)} \qquad (20)$$

where $\epsilon = \frac{Re_D - 47}{47}$. The RMS of the fluctuating lift force predicted from the present analysis is 0.218, which compares well with the approximate value of 0.227 given by equation (20).

Acoustic Source Extraction

Figure 6 shows the time evolution of the acoustic source density at four instances in time. The range is limited to -40 to 40Pa.m^{-2} for clarity. Also, the source density plot at time step = 1 refers to the first time step after the CFD solution has attained periodicity, which has been assigned a time, t=0.0s. Figure 6 shows that significant acoustic sources exist in the vicinity of the cylinder and in the wake of the cylinder.

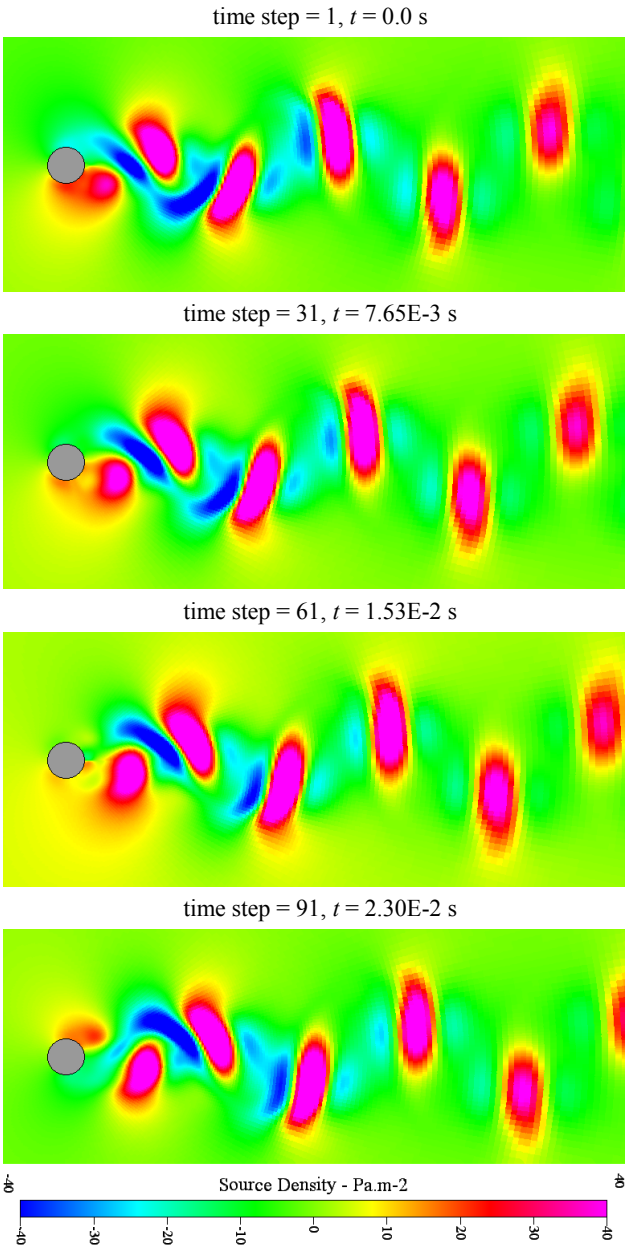

Figure 6. Time evolution of acoustic source density

Figure 7 shows the magnitude and phase of the acoustic source density extracted from the CFD results at the vortex shedding frequency and at the second harmonic. The magnitude plot at the fundamental vortex shedding frequency demonstrates a strong symmetry along the cylinder centreline parallel to the flow direction. The phase plots at this frequency shows a trend that the monopole sources below the centreline are 180° out of phase with the monopole sources above the centreline. This is expected as the fundamental vortex shedding frequency coincides with the first peak of the lift force spectra. The second harmonic of the vortex shedding frequency coincides with the first peak of the drag force spectra. The plot of source density magnitude at the second harmonic of the vortex shedding frequency again exhibits symmetry around the horizontal centreline. However, the phase plot indicates that at this frequency, the acoustic sources on the front of the cylinder are 180° out of phase with those on the back of the cylinder. The region on the cylinder where this phase shift occurs is not at top and bottom dead centre as might be expected, rather the phase shift occurs in the region where the flow separates from the cylinder.

From Figure 7(a), region 1 highlights areas in the cylinder wake where the acoustic sources are caused by vortex shedding from the cylinder. This vortex shedding produces acoustic sources at the fundamental vortex shedding frequency that are equal in magnitude and opposite in phase. This results in 'monopole-monopole cancellation' in the wake region of the cylinder. In the vicinity of the cylinder, this monopole-monopole cancellation is expected to produce pairs of dipole sources aligned vertically, while further downstream the monopole-monopole cancellation will result in a distribution of quadrupole sources. These comments are in line with the findings of Lighthill [2, 3] and Curle [4]. Dipole sources radiate sound more efficiently than quadrupole sources and hence the directivity of the far-field sound pressure should resemble a dipole pattern at the fundamental vortex shedding frequency. Figure 7(b) shows significantly different distributions of magnitude and phase for the monopole sources at the second harmonic of the shedding frequency. At this frequency, the monopole-monopole cancellation will produce pairs of dipole sources aligned horizontally. This is expected to result in the directivity of the far-field sound pressure resembling a dipole pattern aligned front-to-back relative to the cylinder, however this requires further investigation. Region 2 in Figure 7(b) highlights areas where the magnitude and phase of the monopoles for the second harmonic are slightly asymmetric about the horizontal centreline. The cause of this discrepancy is being investigated, however the proximity of region 2 to the far-field boundary suggests the CFD outlet boundary condition may be over-constraining the acoustic sources.

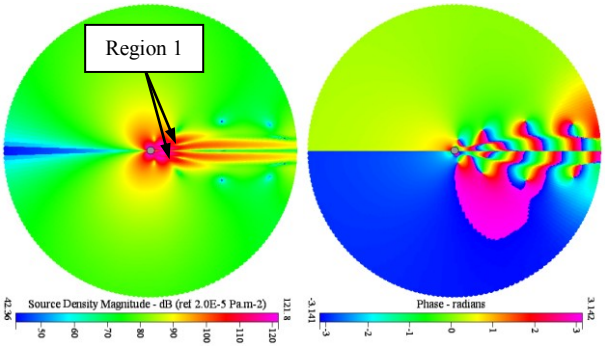

(a) Vortex shedding frequency

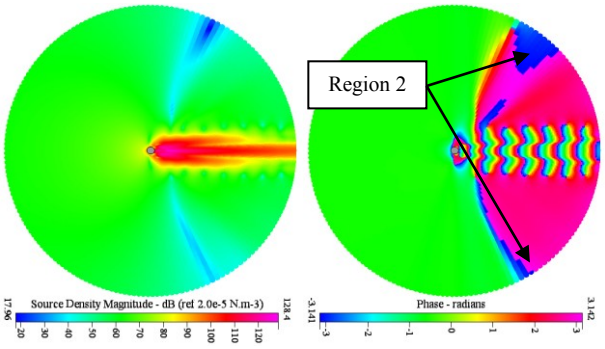

(b) Second harmonic of vortex shedding frequency

Figure 7. Magnitude and phase of acoustic source density

Spatial Condensation of Acoustic Sources

In the present work, only the magnitude and phase of acoustic sources at the vortex shedding frequency are spatially condensed. The method will be extended to higher harmonics in future work. Figures 8 and 9 present the particles in terms of their magnitude and phase. Each particle is rendered by a constant colour depending on the magnitude or phase for that particle. The size of all particles is artificially increased until there is no white space between them. Depending on the particle density this often requires a significant increase in particle size, which can lead to a wavy effect on the far-field boundary. Figure 8 shows the sensitivity of the magnitude and phase of the spatially condensed acoustic sources to the Gaussian kernel shape parameter, σ. For this figure all other particle parameters are held constant at d_c=0.079D, dr=1.05d and l=2.0d, where d_c is the distance separating the particles on the innermost concentric ring. The total number of monopoles produced with this combination of parameters is 4,309, compared with 71,760 without spatial condensation. Figures 8(a) and (b) show that for low values of σ, the magnitude of acoustic sources is not smooth. As the value of σ increases to 0.5, the magnitude plot becomes smooth, as shown in Figure 8(c). Figure 8 also presents the phase of the condensed acoustic sources, which is not sensitive to the value of the smoothing parameter. Figure 8(c) shows that the magnitude and phase of the spatially condensed monopoles has a good match with those of the non-condensed monopoles presented in Figure 7(a). Towards the downstream far-field boundary, the resolution of both magnitude and phase reduces.

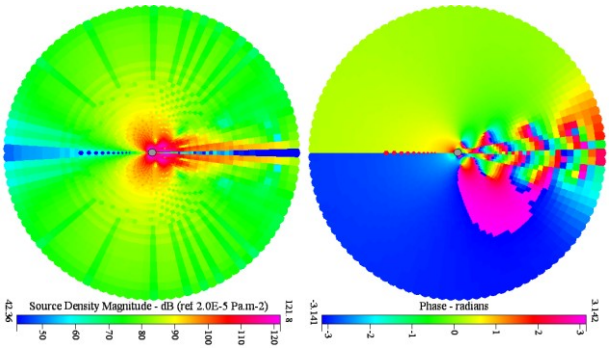

(a) σ = 0.1

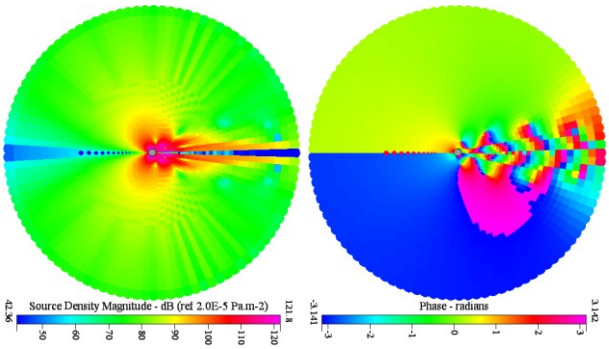

(b) σ = 0.2

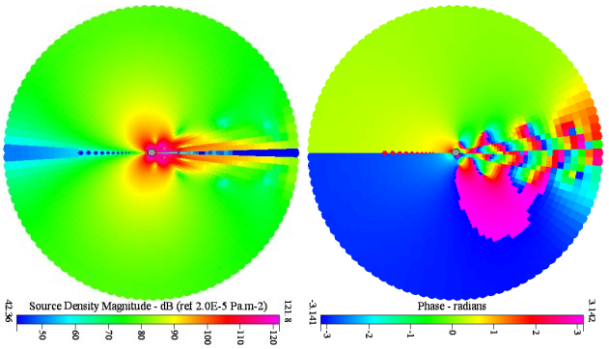

(c) σ = 0.5

Figure 8. Sensitivity of magnitude and phase to kernel shape parameter, σ, at the vortex shedding frequency

Figure 9 presents the sensitivity of the magnitude and phase of the condensed acoustic sources to the change in radius of each ring of particles. For this figure, all other parameters are held

constant at d_c=0.079D, l=2.0d and σ =0.5. Figure 9 shows that both magnitude and phase are heavily influenced by the change in radius between concentric rings of particles. This parameter controls the spatial resolution of the particles. Figure 9(a) shows that the relatively fine spatial resolution achieved with dr=1.025d is able to reproduce the magnitude and phase of the non-condensed monopoles with good accuracy. Even the phase of the condensed monopoles at the downstream boundary closely resembles the phase shown in Figure 7(a). The coarser spatial resolutions shown in Figures 9(b) and (c) are only able to reproduce the magnitude and phase of the non-condensed monopoles in the region around the cylinder. Further downstream the magnitude and phase are not well captured.

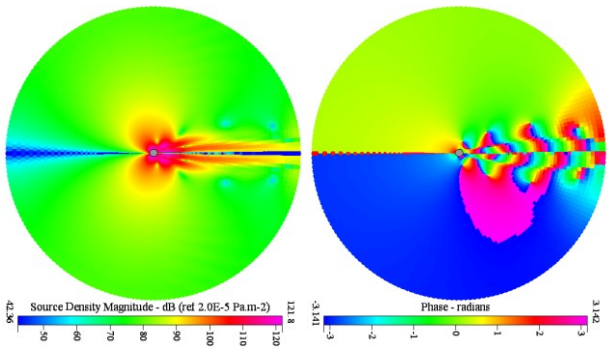

(a) dr = 1.025d, total monopoles = 10,510

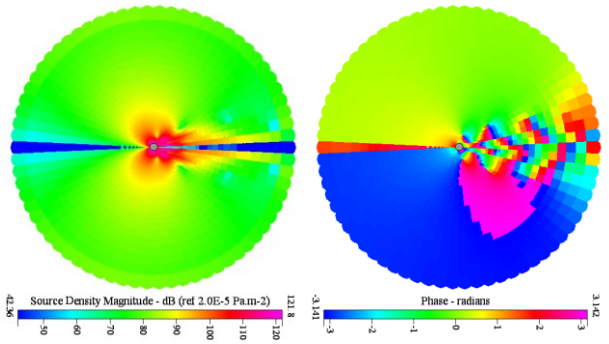

(b) dr = 1.075d, total monopoles = 2,393

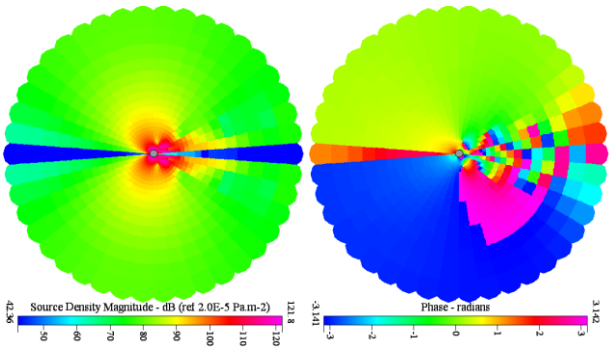

(c) dr = 1.125d, total monopoles = 1,133

Figure 9. Sensitivity of magnitude and phase to change in radius, dr, at the vortex shedding frequency

The particle distributions used in Figures 8 and 9 are symmetric about the horizontal centreline and hence the particles capture the symmetric nature of the magnitude and phase of the non-condensed monopoles. This is true even when the spatial resolution of the particles is poor, as seen in Figure 9(c). Here the magnitude is symmetric about the horizontal centreline and the particles above the centreline are 180° out of phase with those below the centreline, even though the overall patterns are not accurately recreated.

Far-Field Acoustics

The directivity plot of the sound pressure field at the vortex shedding frequency for the non-condensed monopoles is given in Figure 10. This directivity plot is compared with that predicted by Curle's analogy [3]. The data recovery points are placed on a circle of radius 185D centred at 27.25D downstream of the cylinder, which coincides with the front of a propagating and convecting sound wave that is generated at the cylinder. Figure 10 shows that the magnitude of the sound pressure level (SPL) predicted with the present method is greater than that predicted using Curle's analogy, although the directivity of the sound pressure field using both methods are in good agreement. There are several possible causes for the difference in SPL observed in Figure 10. Any vorticity that passes through the outlet boundary of the CFD domain will produce artificially high SPLs [23]. Hence if the sponge layer employed in the present work is not successful at smearing out all of the vorticity before it reaches the far-field boundary, the SPL will be over-predicted. Another possible reason for the discrepancy observed in Figure 10 is that prediction of the propagating acoustic field relies on the complex interaction and cancellation between monopole sources. At low Mach numbers such monopole-monopole interactions are very sensitive with small errors in monopole sources translating into potentially large errors in SPL [23]. These possible sources of error will be investigated in future work.

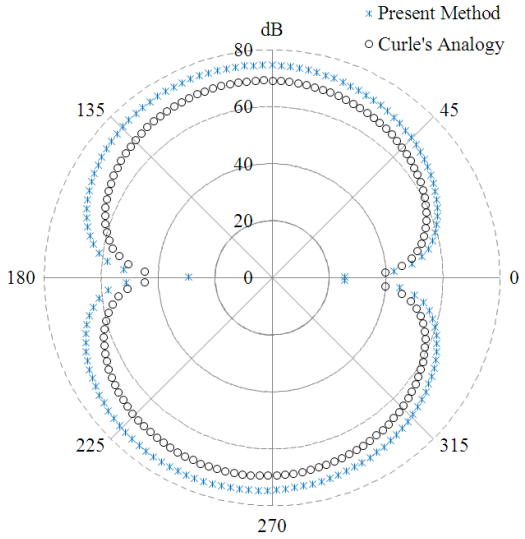

Figure 10. Directivity of sound pressure field at vortex shedding frequency

Figure 11 compares the sound pressure levels predicted with the spatially condensed monopoles depicted in Figure 9, with the sound pressure level from both the non-condensed monopoles and Curle's analogy. For all particle distributions considered, the sound pressure field predicted with the spatially condensed monopoles is very similar to that of the non-condensed monopoles. Figure 12 presents the error between the SPL of the spatially condensed and non-condensed monopoles relative to the SPL predicted by Curle's analogy. Even for the coarsest particle distribution of Figure 9(c), the error in sound pressure level is comparable to the case with non-condensed monopoles. Figure 12 shows a convergence in the results from the spatially condensed monopoles as the number of monopoles increases. Also, as the number of spatially condensed monopoles increases, the error in sound pressure levels relative to those predicted by Curle's analogy decreases. Figure 12 indicates that the results from the spatially condensed monopoles converge to a solution

that is slightly different from the results obtained with the non-condensed monopoles. This suggests that the spatial condensation approach alters the raw acoustic source data. One possible reason is that the spatial condensation method acts as a filter on the raw acoustic source data extracted from the CFD results. Hence any noise in the raw acoustic source time histories will be filtered by the spatial condensation process. This suggests that the raw acoustic source time histories contain noise which may be due to the boundary conditions of the CFD domain and requires further investigation.

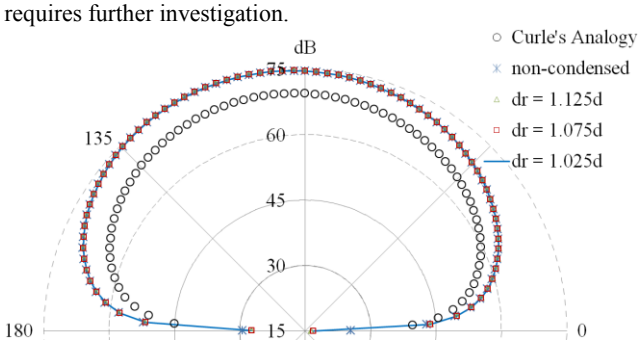

Figure 11. Directivity of sound pressure field from spatially condensed monopoles at vortex shedding frequency

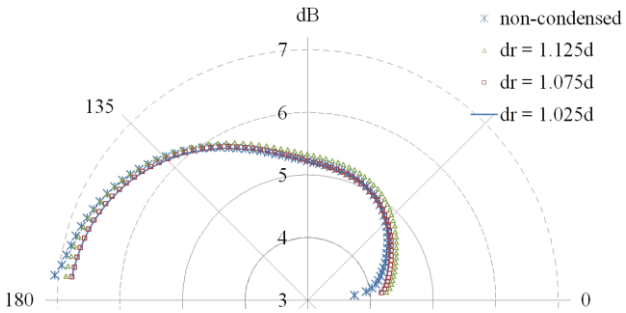

Figure 12. Error of sound pressure directivity predicted at vortex shedding frequency relative to Curle's analogy

Conclusions

A hybrid CFD/BEM approach has been used to predict low Mach number flow induced noise. The method extracts acoustic sources from incompressible CFD data based on the LPCE source terms and then predicts the far field acoustic pressure by solving the harmonic wave equation using a BEM solver. In the present work a method has been developed to spatially condense the acoustic sources and thereby reduce the number of monopoles used in the BEM analysis. For the case considered here, the number of monopoles was reduced by a factor of over 60, with the resulting SPL within 0.5 dB of the non-condensed solution.

The spatial condensation approach is capable of accurately capturing the magnitude and relative phase of the acoustic sources, while at the same time significantly reducing the number of monopoles used in the BEM analysis. The directivity plot at the shedding frequency matches the expected profile well. This is true even for relatively coarse distributions of particles. As the number of spatially condensed monopoles increased, the sound pressure field converged to a slightly different solution than the sound pressure field predicted by non-condensed monopoles. This could be due to the condensation process filtering the raw acoustic source time histories to reduce any noise that is present. The presence of noise in the raw acoustic source data requires further investigation.

Further work is underway to predict the directivity of the sound pressure field at the higher harmonics of the vortex shedding frequency and to assess the accuracy of the spatial condensation approach at these frequencies. It is expected that at higher frequencies, the spatial resolution of particles required to accurately capture the acoustic sources will increase, with the limiting case being a spatial resolution equal to the CFD mesh. An extension to the spatial condensation method is being investigated to overcome this anticipated limitation. This extension will use similar particle distributions overlaid on the CFD mesh. A multipole expansion of all monopoles within the radius of influence of a particular particle will be performed, again weighted by distance using an appropriate kernel. Using this condensed multipole expansion approach, even a relatively coarse particle distribution may be able to take into account the influence of all monopoles.

Acknowledgements

Funding for this work has been provided by the Maritime Platforms Division of the Defence Science and Technology Organisation.

References

1 M.J. Lighthill, "On sound generated aerodynamically, I. general theory", *Proceedings of the Royal Society A*, **211**, 564–587 (1952)

2 M.J. Lighthill, "On sound generated aerodynamically, II. Turbulence as a source of sound", *Proceedings of the Royal Society A*, **222**, 1–32 (1954)

3 N. Curle "The influence of solid boundaries upon aerodynamic sound", *Proceedings of the Royal Society of London A*, **231**, 505–514 (1955)

4 J.E. Ffowcs Williams and D.L. Hawkings, "Sound generation by turbulence and surfaces in arbitrary motion", *Philosophical Transactions of the Royal Society Series A*, **264**, 321–342 (1969)

5 P. di Francescantonio, "A new boundary integral formulation for the prediction of sound radiation", *Journal of Sound and Vibration*, **202**, 491–509 (1997)

6 J.C. Hardin and D.S. Pope, "An acoustic/viscous splitting technique for computational aeroacoustics", *Theoretical and Computational Fluid Dynamics*, **6**, 323–340 (1994)

7 R. Ewert and W. Schröder, "Acoustic perturbation equations based on flow decomposition via source filtering", *Journal of Computational Physics*, **188**, 365–398 (2003)

8 J.H. Seo and Y.J. Moon, "Perturbed compressible equations for aeroacoustic noise prediction at low Mach numbers", *AIAA Journal*, **43**, 1716-1724 (2005)

9 J.H. Seo and Y.J. Moon, "Linearized perturbed compressible equations for low Mach number aeroacoustics", *Journal of Computational Physics*, **218**, 702–719 (2006)

10 J.H. Seo and Y.J. Moon, "Aerodynamic noise prediction for long-span bodies", *Journal of Sound and Vibration*, **306**, 564–579 (2007)

11 P. Croaker, R. Kinns, N. Kessissoglou, D. Norrison, R. Widjaja and S. Marburg, "Hybrid CFD/BEM approach to predict flow induced noise", In *Proceedings of the 20th International Congress on Acoustics,* Sydney, Australia, 23-27 August 2010

12 H.S. Ribner, "New theory of jet-noise generation, directionality and spectra", *Journal of Acoustical Society of America*, **31**, 245-246 (1959)

13 *CFD-ACE+ V2009.4 User Manual*, ESI Group, Paris, France 2009

14 I. Orlanski, “A simple boundary condition for unbounded hyperbolic flows”, *Journal of Computational Physics*, **21**, 251–269 (1976)

15 M. Breuer, “Numerical and modeling influences on large eddy simulations for the flow past a circular cylinder”, *International Journal of Heat and Fluid Flow*, **19**, 512–521 (1998)

16 M. Breuer, “A challenging test case for large eddy simulation: high Reynolds number circular cylinder flow”, *International Journal of Heat and Fluid Flow*, **21**, 648–654 (2000)

17 *VA One 2010 User's Guide*, ESI Group, Paris, France, June 2010

18 P.D. Welch, “The use of fast Fourier transform for the estimation of power spectra: a method based on time averaging over short, modified periodograms”, *IEEE Transactions on Audio Electroacoustics*, **15**, 70–73 (1967)

19 W.H. Press, S.A. Teukolsky, W.T. Vetterling, and B.P. Flannery”, *Numerical Recipes in Fortran (The Art of Scientific Computing)*, Cambridge Unviersity Press, Cambridge, 2nd edition, 1992

20 D.J. Tritton, “Experiments on the flow past a circular cylinder at low reynolds numbers”, *Journal of Fluid Mechanics*, **6**, 547–567 (1959)

21 U. Fey, M. König, and H. Eckelmann, “A new Strouhal–Reynolds-number relationship for the circular cylinder in the range $47<Re<2\text{x}10^5$”, *Physics of Fluids*, **10**, 1547–1549 (1998)

22 C. Norberg “Flow around a circular cylinder: Aspects of fluctuating lift”, *Journal of Fluids and Structures*, **15**, 459-469 (2001)

23 M. Wang, J.B. Freund, and S.K. Lele “Computational prediction of flow-generated sound”, *Annual Review of Fluid Mechanics*, **38**, 483-512 (2006)